Additive Manufacturing 59 (2022) 103080

Contents lists available at ScienceDirect

Additive Manufacturing

journal homepage: www.elsevier.com/locate/addma

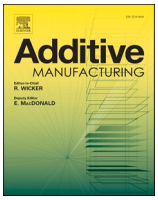

Role of build orientation on quasi-static and dynamic fracture responses of additively manufactured AlF357 and AlSi10Mg alloys

John P. Isaac [a], Seungjong Lee [a,b], Spencer Thompson [c], Ankit Saharan [c], Nima Shamsaei [a,b], Hareesh V. Tippur [a,*]

[a] Department of Mechanical Engineering, Auburn University, AL 36849, USA
[b] National Center for Additive Manufacturing Excellence, Auburn University, AL 36849, USA
[c] EOS North America, 3813 Helios Way #B298, Pflugerville, TX 78660, USA

ARTICLE INFO

Keywords:
Aluminum alloys
Laser-powder bed fusion (L-PBF/LB-PBF)
Fracture mechanics
High strain-rate behavior
Digital Image Correlation

ABSTRACT

In this work, a popular additive manufacturing (AM) aluminum alloy - AlSi10Mg and a new AM aluminum alloy - AlF357 are fabricated using Laser-Powder Bed Fusion (L-PBF) approach to evaluate quasi-static and dynamic fracture behaviors. Four build orientations - horizontal, vertical, flat, and diagonal - are assessed. A Kolsky pressure bar apparatus along with ultrahigh speed photography is used to carry out the dynamic fracture experiments. In-plane surface displacements near cracks are measured using Digital Image Correlation (DIC) to evaluate the fracture parameters directly. A hybrid experimental-numerical approach that combines DIC measurements and finite element analysis is implemented to extract critical energy release rate and crack growth resistance behaviors. The effect of build orientation is found to be significant on the quasi-static fracture behavior with the horizontal and flat orientations having the best and worst fracture responses, respectively. Under dynamic loading conditions, however, the effects of build orientation are marginal. Both AlF357 and AlSi10Mg show strain-rate sensitivity and change in fracture mechanism under dynamic loading conditions with ~175% and ~200% increase in critical energy release rate. AlF357 consistently outperforms AlSi10Mg in both quasi-static (~30%) and dynamic (~10%) loading conditions.

1. Introduction

Additive manufacturing (AM) alloys have found themselves employed in numerous safety-critical areas including aerospace, biomedical, and automotive industries [1–4]. With the advent of additive manufacturing, significant effort has been made to manufacture aluminum (Al) alloys additively [5,6]. Al alloys are highly desirable in engineering applications for their excellent properties including high specific strength, corrosion resistance, and excellent machinability, among others [7–9]. Among the traditional Al alloys, AlSi10Mg is one of the popular commercially available alloys used for AM. AlSi10Mg is well suited for the laser-powder bed fusion (L-PBF) process as it exhibits good fluidity, low shrinkage, and a small solidification range [10–13]. During the L-PBF process, the AM materials undergo rapid melting and solidification. AlSi10Mg possesses a low coefficient of thermal expansion among Al alloys, which allows it to be manufactured with better dimensional accuracy and reduced thermal stresses [14]. Apart from adopting traditional materials in AM, new metallic alloys have been in development to be used for AM exclusively [5,15]. AlF357, from the family of cast A356 alloy, is introduced by EOS- an L-PBF machine manufacturer, and is specifically designed for AM processes [16]. With the ever-increasing potential of printable Al alloys for fracture-critical applications, it is critical to investigate the effects of AM-introduced artifacts on the mechanical behavior of Al parts in general and fracture behavior in particular.

Currently, a few published reports on tensile and strain-rate sensitivity behaviors of additively manufactured (AM) AlSi10Mg can be found in the literature. The tensile strength and hardness values of AlSi10Mg produced by the L-PBF process were studied and compared with those of conventionally cast AlSi10Mg in Ref. [17]. The results showed that the AM parts had higher strength and hardness owing to the

Abbreviations: AM, Additive Manufacturing/Additively Manufactured; L-PBF, Laser- Powder Bed Fusion; DIC, Digital Image Correlation; FE, Finite Element; SEM, Scanning Electron Microscope/Microscopy; EBSD, Electron Back Scatter Diffraction; ROI, Region of Interest; FPS, Frames Per Second; YS, Yield Strength; UTS, Ultimate Tensile Strength; XCT, X-ray Computed Tomography.

* Corresponding author.
E-mail address: tippuhv@auburn.edu (H.V. Tippur).

https://doi.org/10.1016/j.addma.2022.103080
Received 28 April 2022; Received in revised form 21 July 2022; Accepted 8 August 2022
Available online 10 August 2022

Nomenclature

Al	Aluminum.
u	Crack opening displacement.
v	Crack sliding displacement.
E	Modulus of Elasticity.
ν	Poisson's ratio.
J	Energy release rate.
a	Crack length.
XYZ	Build-plate coordinate system.
xyz	Crack-tip coordinate system.
r	Radial distance from crack tip.
B	Specimen thickness.

Table 1
Chemical compositions for AlF357 and AlSi10Mg as reported by the manufacturer.

Element	AlF357 Weight %	AlSi10Mg
Silicon (Si)	6.5–7.5	9–11
Iron (Fe)	0.1 max	< 0.55
Copper (Cu)	0.2 max	< 0.05
Manganese (Mn)	0.1	< 0.45
Magnesium (Mg)	0.4–0.7	0.2–0.45
Nickel (Ni)	–	< 0.05
Zinc (Zn)	0.1 max	< 0.10
Lead (Pb)	–	< 0.05
Tin (Sn)	–	< 0.05
Titanium (Ti)	0.04–0.2	< 0.015
Beryllium (Be)	< 0.002	–
Aluminum (Al)	Balance	
Minimum Particle Size	20 μm	20 μm
Maximum Particle Size	90 μm	63 μm
Powder Manufacturer	EOS	

finer microstructure and distribution of the silicon phase in the alloy. The influence of post-processing (hot isostatic pressing and T6 heat-treatment) and the effect of the build orientation on the tensile properties for L-PBF AlSi10Mg alloy were studied in Ref. [18]. The results showed that specimens that were as-fabricated, T6-only, and hot isostatic pressing with T6 combined all had higher yield strength (YS) and ultimate tensile strength (UTS) than cast counterparts (T6). Horizontally built specimens were better in YS and UTS than vertically built ones due to the orientation of detrimental lack of fusions in the vertical orientation. The effects of build orientation and heat-treatment on the quasi-static fracture toughness of AlSi10Mg manufactured by the L-PBF process were investigated in Ref. [19]. Three build orientations (horizontal, diagonal, and vertical) and three heat-treatments (stress-relieved (SR), homogenization followed by aging protocol-1 (HA-1), and homogenization followed by aging protocol-2 (HA-2)) were considered. The SR specimens showed the highest fracture toughness. The fracture toughness among build orientations was the highest for horizontal, then the diagonal orientation; the vertical orientation had the least toughness in the as-built, HA-1, and HA-2 conditions.

The strain-rate sensitivity of AlSi10Mg alloy fabricated by L-PBF was investigated by performing tension experiments in strain-rates ranging from 2.77×10^{-6} to 2.77×10^{-1} s^{-1} in Ref. [20]. The results indicate that L-PBF parts were strain-rate sensitive with an increase in strain-rate leading to a significant increase in flow stress and strain hardening exponents. The dynamic tensile response of different build orientations for L-PBF AlSi10Mg was studied and compared with that of sand cast ones in Ref. [21]. It was observed that the dynamic response was independent of the orientation and the dynamic YS was twice that of sand cast AlSi10Mg. The increase in YS was attributed to the higher homogeneity of the microstructure of L-PBF parts. Interestingly, the fracture mode was found to change from ductile to brittle at strain-rates greater than 5×10^{3} s^{-1}. A few other works with similar results on the strain-rate sensitivity and relatively brittle behavior under dynamic tensile and compressive loading have been published recently [22–24]. However, since AlF357 is a newer Al alloy, the only literature available is on the fatigue behavior of L-PBF AlF357 [16]. Nezhadfar et al. investigated and compared the fatigue behavior of five different Al alloys (AlF357, AlSi10Mg, Scalmalloy, QuesTek Al, and AD1) fabricated by L-PBF. The effect of build orientation (horizontal and vertical) was explored as well. The fatigue behavior results indicated that AlSi10Mg did not have significant build orientation dependency while AlF357 exhibited anisotropic behavior in the high cycle fatigue regime. In addition, AlF357 was reported to have a higher stress-life fatigue behavior at 0.003 mm/mm than AlSi10Mg.

To the authors' knowledge, no work has been reported on the fracture mechanics of L-PBF AM AlSi10Mg and AlF357 alloys extensively under static and dynamic loading conditions. Therefore, it is important to explore the effects of AM-induced artifacts which could potentially dictate the fracture behavior of the parts. In addition, the use of AM parts in fracture-critical applications warrants studying the behavior under different loading rates. Hence, the effect of build orientations and loading rate on the fracture behavior of L-PBF AlF357 and AlSi10Mg alloys has been studied in this work. Four different build orientations and two different loading rates are considered. The optical method of Digital Image Correlation (DIC) [25] has been utilized to obtain the local in-plane surface deformations during fracture experiments. The use of DIC allows quantification of the local displacement fields in two orthogonal directions near the crack tip during the fracture event. Further, a methodology in which experimentally measured displacements from DIC is exported to a companion Finite Element (FE) model to extract desired fracture property namely, the energy release rate (or the J-integral), has been implemented in this work. This hybrid DIC-FE approach has been successfully shown in fracture studies ranging from polymers to metal alloys under both quasi-static and dynamic loading conditions [26–29].

Following this introduction, details on specimen fabrication including build orientations are provided. Experimental descriptions of quasi-static fracture tests, dynamic fracture tests, and microscopy follow. Subsequently, the fracture results are described. It is then followed by a discussion of the results before concluding the article with the major findings of this work. An appendix containing information on hybrid DIC-FE methodology and data extraction approach is included as well for completeness.

2. Experimental details

2.1. Specimen fabrication and geometry

The chemical composition of aluminum AlF357 and AlSi10Mg powders comply with SAE AMS 4289 and DIN EN 1706 standards, respectively. The chemical compositions reported by the manufacturer are listed in Table 1 [30,31]. All AlF357 and AlSi10Mg specimens were fabricated by an EOS M290 L-PBF system using default process parameters developed by the manufacturer for each material. For AlF357 and AlSi10Mg alloys, EOSPRINT 2.6 (AlF357_030_M291 1.00) and EOSPRINT 2.6 (AlSi10Mg_SpeedM291 1.20) were used as the defined parameter set, respectively.[1] The recoater blade was an EOS HSS rake and the layer thickness was 30 μm for both materials. The inert gas used was nitrogen for AlF357 but argon for AlSi10Mg. After printing, both build plates along with the specimens were directly stress relieved by

[1] The specifics associated with laser power, scan speed, spot size, etc. are proprietary and can be obtained directly from EOS, North America.

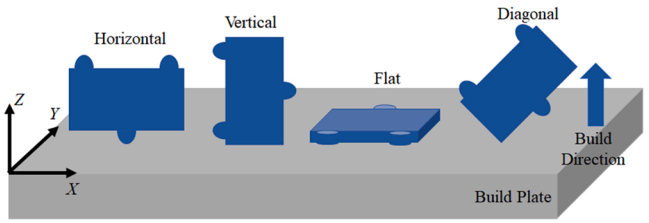

Fig. 1. Schematic illustration of build orientations with respect to the build plate.

preheated argon gas at 270 °C for 100 min (extra 10 min for parts to reach 270 °C). After the stress relief step, specimens were removed from the build plate by wire electrical discharge machining and were tested in the as-built condition.

Both the quasi-static and dynamic specimens were printed in four different build orientations namely, horizontal, vertical, flat, and diagonal. Fig. 1 illustrates the build orientation for each type of specimen with respect to the build plate. The horizontal orientation was placed on the build plate in such a way that the longer dimension of the specimen was parallel to the build plate. For the vertical orientation, the longer dimension was perpendicular to the build plate, while for the diagonal orientation, the longer dimension was at 45° to the build plate. The other build orientation was the flat orientation, in which one of the surfaces on the specimen was directly laid on the build plate itself.

2.2. Quasi-static fracture tests

Quasi-static fracture experiments were carried out using an Instron 4465 mechanical tester fitted with a 5 kN load cell. Fig. 2(a) shows the geometry of specimens used for quasi-static tests. The specimens were printed to the required dimensions with the help of supports and the supports were removed after the stress-relieving step. A crack of length 5 mm and width 150 μm was inserted into one of the two long specimen edges at the mid-span using a diamond circular saw. The specimens were loaded in a three-point bending configuration and displacement control mode at a crosshead speed of 0.005 mm/s using roller pin supports. Load, time, and crosshead displacement were all recorded during each experiment. Prior to the start of the experiment, the specimen surfaces were sprayed with fine mists of black and white paint to create random speckles to facilitate 2D-DIC measurements and quantify surface deformations. A PointGrey camera (2048 ×2048 pixels) fitted with an 18–208 mm focal length macro zoom lens was used to capture the images at 2 frames per second (fps). Speckle images were captured starting from the undeformed state of the specimen to crack initiation and crack propagation of approximately 4 mm.

2.3. Dynamic fracture tests

Fig. 2(b) shows the geometry of specimens used for high strain-rate fracture experiments. The geometry consisted of circular pins printed during AM process to load specimens in a symmetric three-point bend configuration. This design was favored over integrating pins into the incident and the transmitter bars of the Kolsky bar apparatus for simplicity. The strategy of performing full-field optical measurements directly on specimens facilitated this approach even though pins themselves deform during the loading event. A crack of 5 mm in length and 150 μm in width was inserted into each of the specimens using a circular diamond saw cutter. The dynamic fracture specimens were then sprayed with mists of black and white paint to create random speckles on one of the two surfaces to perform DIC-based measurement and quantify in-plane deformations. A Kirana-05 M ultrahigh-speed camera (924 ×768 pixels) fitted with an 80–400 mm focal length lens and adjustable bellows (Nikon PB6) was used to record time-resolved surface deformations at a rate of 200,000 fps. A compression Kolsky bar apparatus was used for high strain-rate loading (strain rate ~500 s^{-1}) by subjecting the specimens to stress-wave loadings. The schematic diagram of the loading apparatus and the arrangement for recording speckles are shown in Fig. 3.

The Kolsky bar apparatus consisted of two long bars of length 2.4 m and diameter of 25.4 mm made of C350 maraging steel used as the incident and transmission bars. A maraging steel striker rod of length 305 mm and diameter 25.4 mm was launched from a gas gun barrel to

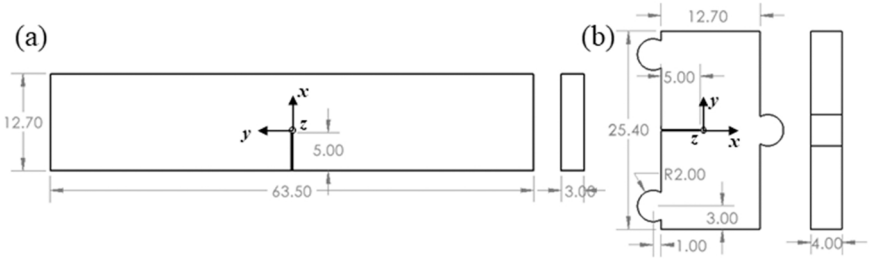

Fig. 2. Specimen geometry for (a) quasi-static and (b) dynamic experiments. All dimensions are in mm.

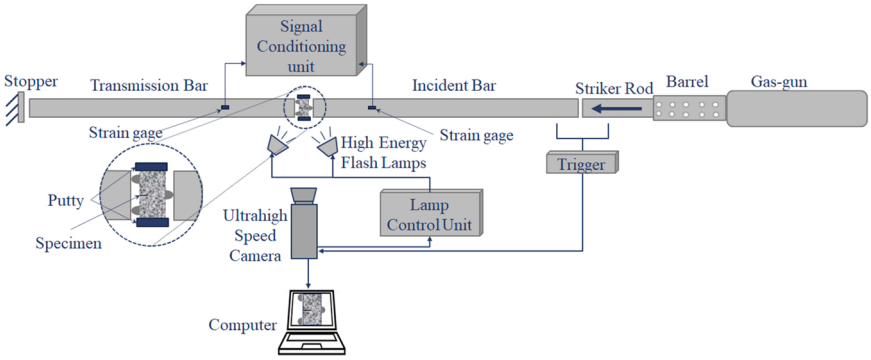

Fig. 3. Schematic representation of the compression Kolsky bar apparatus used for dynamic loading.

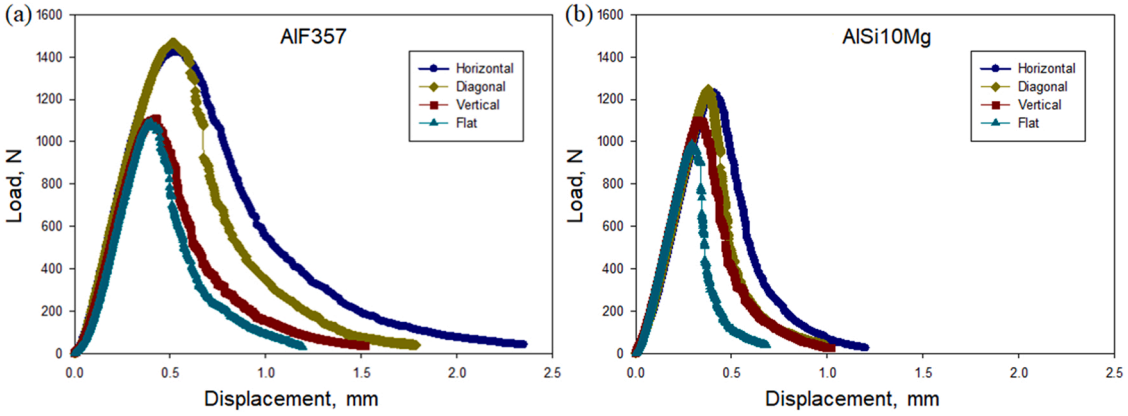

Fig. 4. Load vs. load-point deflection for (a) AlF357 and (b) AlSi10Mg specimens under quasi-static loading.

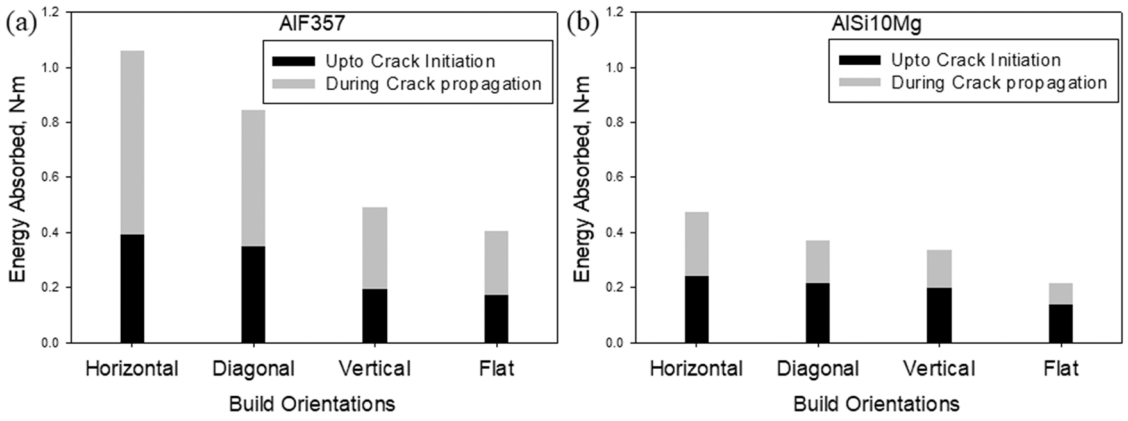

Fig. 5. Energy absorbed by (a) AlF357 and (b) AlSi10Mg specimens under quasi-static loading before and after crack initiation.

impact the incident bar co-axially and generate stress waves. The other end of the incident bar had a flat profile and was in contact with the central loading pin of the specimen opposite to the crack tip. The other edge of the specimen with two loading pins was in contact with the flat profile of the transmission bar. All three loading pins were kept in contact with the two long bars before the start of the loading event. To hold the specimen between the two bars and prevent it from slipping down due to gravity during alignment, a block of soft putty was used as a support. The low acoustic impedance of the putty block provided an approximately free support condition. For acoustic symmetry relative to the loading axis, another putty block was pressed on the top edge of the specimen as well. In all experiments, the maraging steel striker was launched at a velocity of ~40 m/s to impact the incident bar.

2.4. Microstructure assessment and fractography

In this work, the macroscale fracture performance of specimens was examined relative to microstructural features and via fractography. The details of the steps involved in that phase of work are as follows: The specimens from each build orientation were cut in three different planes (i.e., *x-y, y-z,* and *x-z* planes) relative to the crack tip coordinates (see, Fig. 2). According to ASTM E3 guidelines for preparing metallographic specimens, specimens were mechanically ground using silicon carbide grinding papers with different grit sizes from P320 to P4000, then mechanically polished using 0.05 μm colloidal silica suspension on a polishing cloth (ChemoMet provided by Buehler). In addition, the specimens were polished in a vibratory polisher using 0.02 μm colloidal silica suspension to obtain a mirror-like surface finish. Electron backscatter diffraction (EBSD) analysis was carried out on polished specimens in a Zeiss Crossbeam 550 scanning electron microscope (SEM) to characterize the microstructure. A grain size analysis was carried out using Aztec, a post-process software from Oxford Instrument.

X-ray computed tomography (XCT) was performed to investigate porosity distribution in horizontally and vertically fabricated quasi-static AlF357 and AlSi10Mg specimens in a Zeiss Xradia 620 Versa system. The test parameters were as follows: voltage = 70 kV, current = 8.5 W, voxel size = 3.46 μm, and exposure time = 5 s. The XCT data was reconstructed by the software provided by the equipment manufacturer and stored as TIFF images. Further image processing was conducted using ImageJ and Dragonfly software.

The fractured surfaces after both quasi-static and dynamic tests were also examined using Zeiss Crossbeam 550 SEM. The crack initiation sites were especially investigated in the SEM at high magnification to determine crack initiation mechanisms.

3. Experimental results

3.1. Quasi-static fracture tests

Load versus load-point deflection responses for three-point bending fracture experiments of all the four build orientations under quasi-static loading are shown in Fig. 4. Three specimens were tested in each condition and the response with the highest peak load in each condition is shown in Fig. 4. They all show a linear response almost until the peak load (i.e., crack initiation). Subsequently, a gradual drop in the load was observed in each case as the crack propagated. From the responses of AlF357 shown in Fig. 4(a), considering the peak load and response during crack propagation, it can be observed that the horizontal orientation had the best failure response with higher peak load and energy dissipation. This was closely followed by the diagonal orientation. The

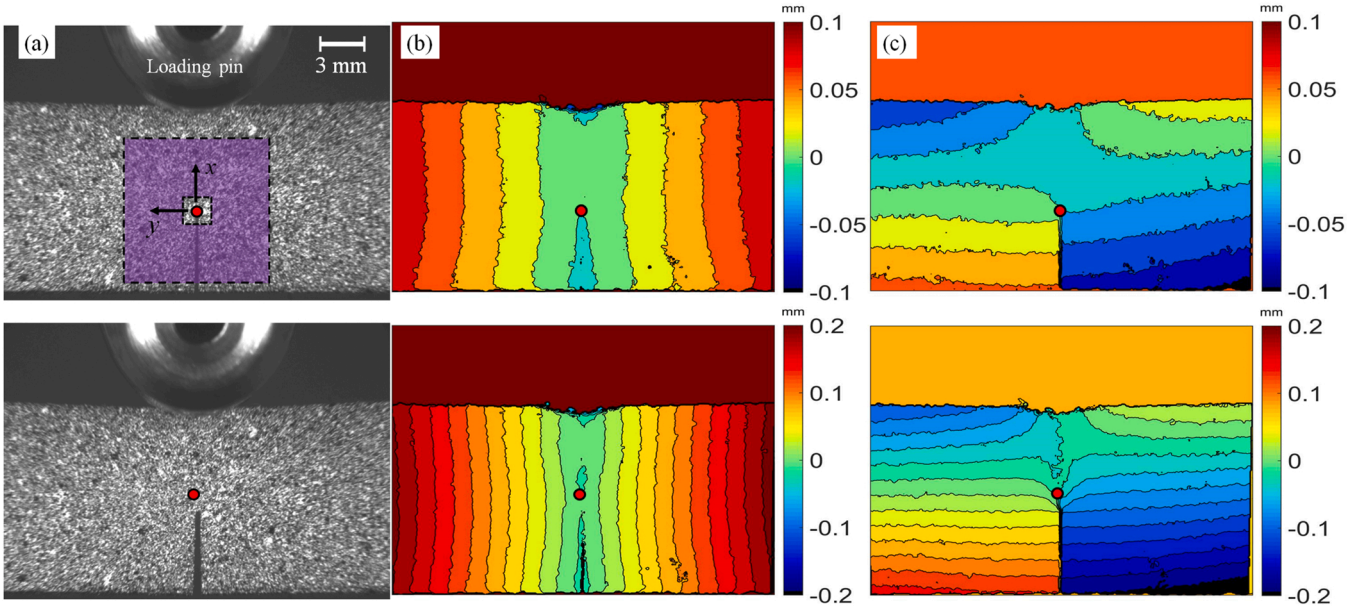

Fig. 6. Optical measurements for a horizontally built AlSi10Mg specimen under quasi-static loading. (a) Speckle images, (b) *x*- or *u*-field, and (c) *y*- or *v*-field displacement contours. The top (1000 N) and bottom (1200 N) rows correspond to time steps before and after crack initiation. Red solid dots correspond to the crack tip location.

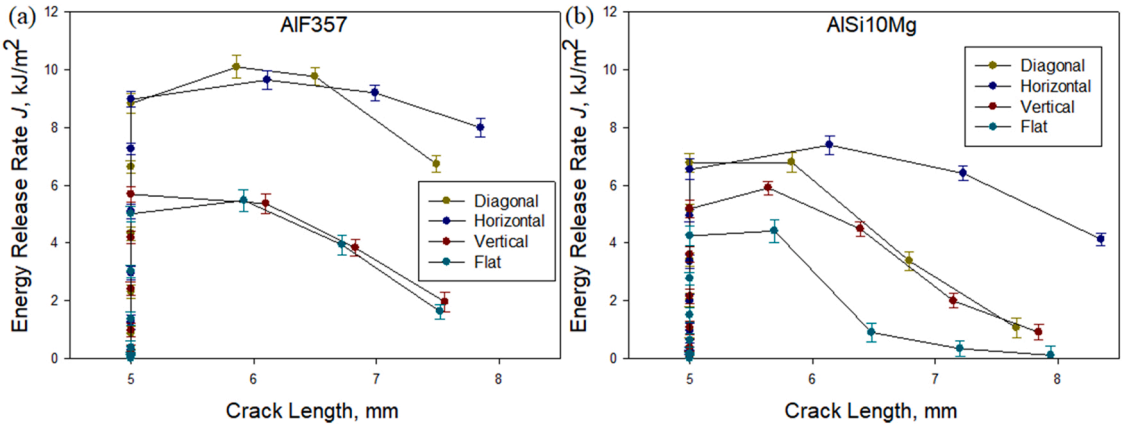

Fig. 7. Quasi-static crack growth resistance curves for (a) AlF357 and (b) AlSi10Mg alloys for the four different build orientations.

vertical and flat orientations had similar responses but the peak loads were noticeably lower when compared to the former two orientations. That is, the horizontal and diagonal orientations had a ~30% higher critical load, or load at crack initiation when compared to the vertical and flat orientations. The load versus load-point deflection curves for AlSi10Mg are shown in Fig. 4(b). Similar to the results for AlF357, considering the peak load and material response during crack propagation, the horizontal orientation had the best response (i.e., the highest critical load) closely followed by the diagonal orientation. The vertical orientation had the next best response and the flat orientation had the worst response for AlSi10Mg. The horizontal and diagonal orientations had ~25% higher critical load when compared with the flat orientation, while the vertical orientation had ~11% higher value when compared to the flat orientation.

To further quantify these responses during crack propagation, the energy absorbed by each orientation was computed as the area under the curve before and after crack initiation and the results are shown as histograms in Fig. 5. Note that for the crack propagation region, the energy absorbed was computed until the load dropped to 250 N in each case. Results indicate that the horizontal orientation absorbs the most energy during crack propagation compared to other build orientations for both AlF357 and AlSi10Mg alloys. The flat orientation had the worst response among the four build orientations studied. In AlF357 alloy, horizontal orientation (0.67 ± 0.03 N-m), diagonal orientation (0.49 ± 0.03 N-m), and the vertical orientation (0.30 ± 0.03 N-m) had ~190%, ~115%, ~30% increase in energy absorption during crack growth when compared to the flat orientation (0.23 ± 0.02 N-m) respectively. In AlSi10Mg alloy, the horizontal orientation (0.23 ± 0.02 N-m), diagonal orientation (0.16 ± 0.02 N-m), and the vertical orientation (0.13 ± 0.03 N-m) had ~200%, ~100%, and ~80% increase in energy absorption during crack growth compared to the flat orientation (0.07 ± 0.02 N-m) respectively. Among the two Al alloys, clearly, AlF357 absorbed considerably more energy (~190%, ~210%, ~110%, and ~190% for the horizontal, diagonal, vertical, and flat orientations respectively) than AlSi10Mg during crack propagation under quasi-static loading.

The recorded speckle images from the camera were correlated using an image analysis software, ARAMIS®. The speckle images at no-load condition were used as reference images to correlate with the images in the deformed state at different time instants or load steps during the

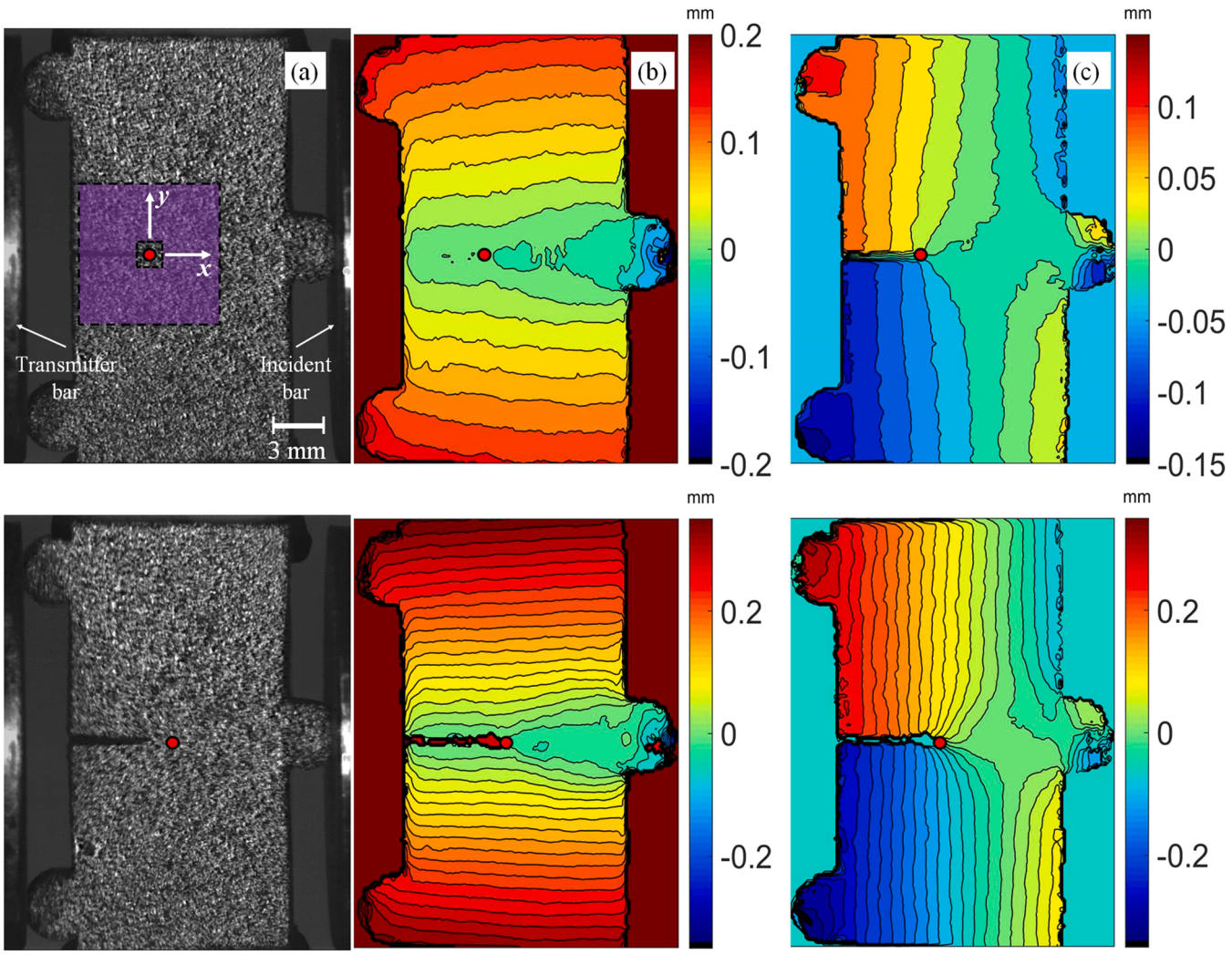

Fig. 8. Surface deformations for a horizontally built AlSi10Mg specimen under dynamic loading. (a) Speckle images at time $t = -15$ μs (top row) and $t = 15$ μs (bottom row). (b) x- or u-field, (c) y- or v-field displacement contours. Red solid dots indicate the crack tip location.

event to obtain instantaneous displacement component fields in two orthogonal directions, along (x) and perpendicular (y) to the initial crack orientation. A square sub-image size of 25 pixels and a step size of 5 pixels was used while performing image correlation. An example of a pair of displacement contours along with their respective speckle images before and after crack initiation is shown in Fig. 6 for the horizontally built AlSi10Mg specimen. The displacement contours are plotted at an increment of 20 μm. The top row corresponds to a load step before crack initiation and the bottom row corresponds to a load step during crack propagation. Symmetric contours with respect to the crack and loading axis can be observed in the x- or the u-field whereas antisymmetric contours in the y- or the v-field around the crack tip. Globally, the far-field deformation fields correspond to the ones dominated by bending. As noted earlier, a hybrid DIC-FE methodology was adopted to extract the crack tip parameters and the details of the methodology and analysis are included in Appendix A. The region from where the J-integral values were extracted in the quasi-static experiments is highlighted in the speckle image as a shaded region, see Fig. 6(a).

Quasi-static crack growth resistance curves for both aluminum alloys are shown in Fig. 7. For AlF357 alloy (Fig. 7(a)), the horizontal orientation was found to have the highest value of critical energy release rate (or energy release rate at crack initiation) at 8.9 kJ/m^2, followed by the diagonal orientation at 8.8 kJ/m^2. These two are followed by the vertical orientation at 5.7 kJ/m^2 and the flat orientation was found to have the least critical energy release rate at 5.1 kJ/m^2. Upon observing the entire fracture behavior, it can be seen that the horizontal and diagonal build orientations had similar responses. It is also notable that the vertical and flat orientations had similar behaviors. These are consistent with the load versus load-point deflection plots reported in Fig. 4. However, for all build orientations, the variation of energy release rate with crack growth, dJ/da, immediately after crack initiation was approximately constant indicating a stable crack growth behavior. After some amount of stable crack growth, however, dJ/da values become negative suggesting an unstable crack growth.

For AlSi10Mg alloy (Fig. 7(b)) on the other hand, the critical energy release rate was the highest for the horizontal orientation at 6.7 kJ/m^2, followed by the diagonal orientation at 6.5 kJ/m^2, then the vertical at 5.2 kJ/m^2, and finally the flat orientation at 4.3 kJ/m^2. When it comes to crack propagation behavior, all build orientations in AlSi10Mg exhibit similar trends, where $dJ/da \sim 0$ right after crack initiation, followed by immediate unstable crack growth. Overall, AlF357 alloy outperformed AlSi10Mg with the horizontal build orientation seeming to be the best build orientation in both cases under quasi-static conditions. Three specimens in each condition were tested to ensure repeatability and the standard deviation in the quasi-static experiments was $\pm$ 0.4 kJ/m^2.

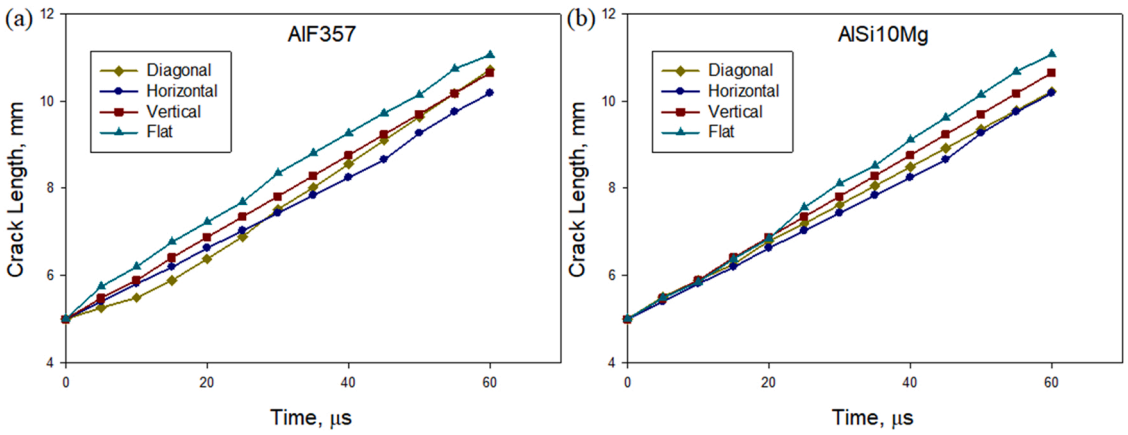

Fig. 9. Crack length histories for (a) AlF357 and (b) AlSi10Mg alloys under dynamic loading.

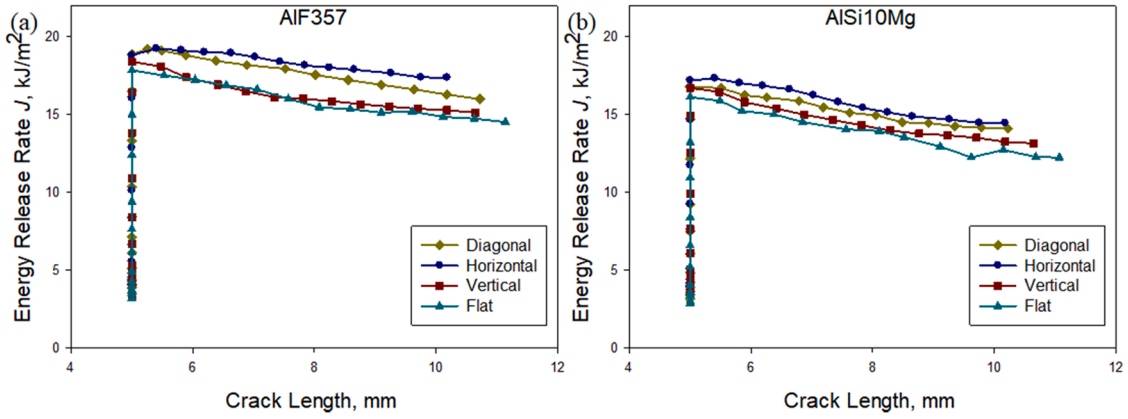

Fig. 10. Crack growth resistance curves for (a) AlF357 and (b) AlSi10Mg alloys under dynamic loading.

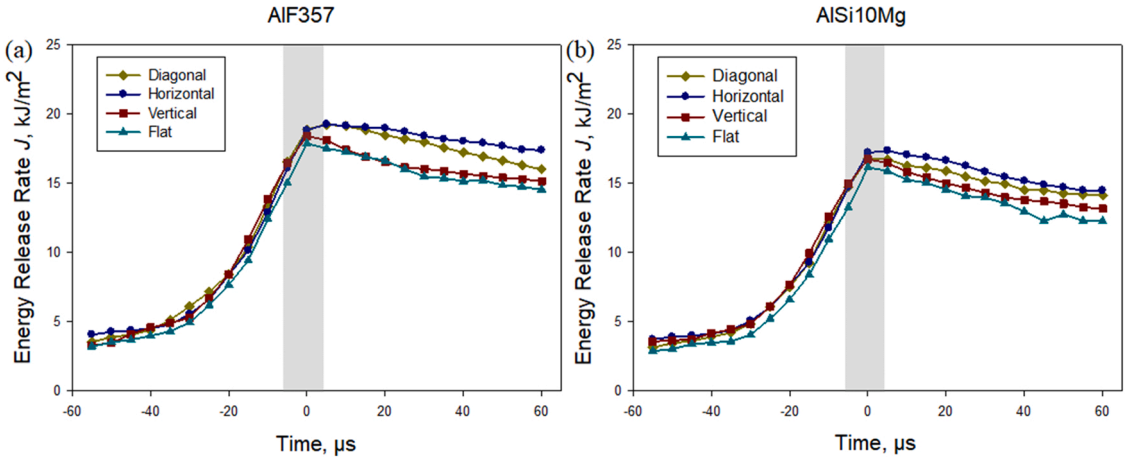

Fig. 11. *J*-integral histories for (a) AlF357 and (b) AlSi10Mg alloys under dynamic loading. Negative and positive time scales correspond to pre- and post- crack initiation regimes. The gray band centered on $t = 0$ μs refers to the approximate crack initiation instant.

3.2. Dynamic fracture tests

The surface of specimens decorated with a random speckle pattern was photographed at 200,000 fps during rapid stress-wave loading events in the Kolsky bar apparatus. Subsequently, the images in the deformed state were correlated with a reference image in the undeformed state from that experiment during the post-processing step. The temporal evolution of displacement contours in two orthogonal directions was obtained for each experiment. A square sub-image size of 25 pixels and a step size of 5 pixels was used during image analysis in ARAMIS®. An example set of displacement fields plotted at 20 μm increments is shown in Fig. 8. The speckle images and displacement contours shown correspond to a horizontally built AlSi10Mg specimen. The top and bottom rows correspond to time steps before and after crack initiation. In the top row, *x*- or the *u*-field, it can be observed that the contours are symmetric in shape and magnitude relative to the crack and

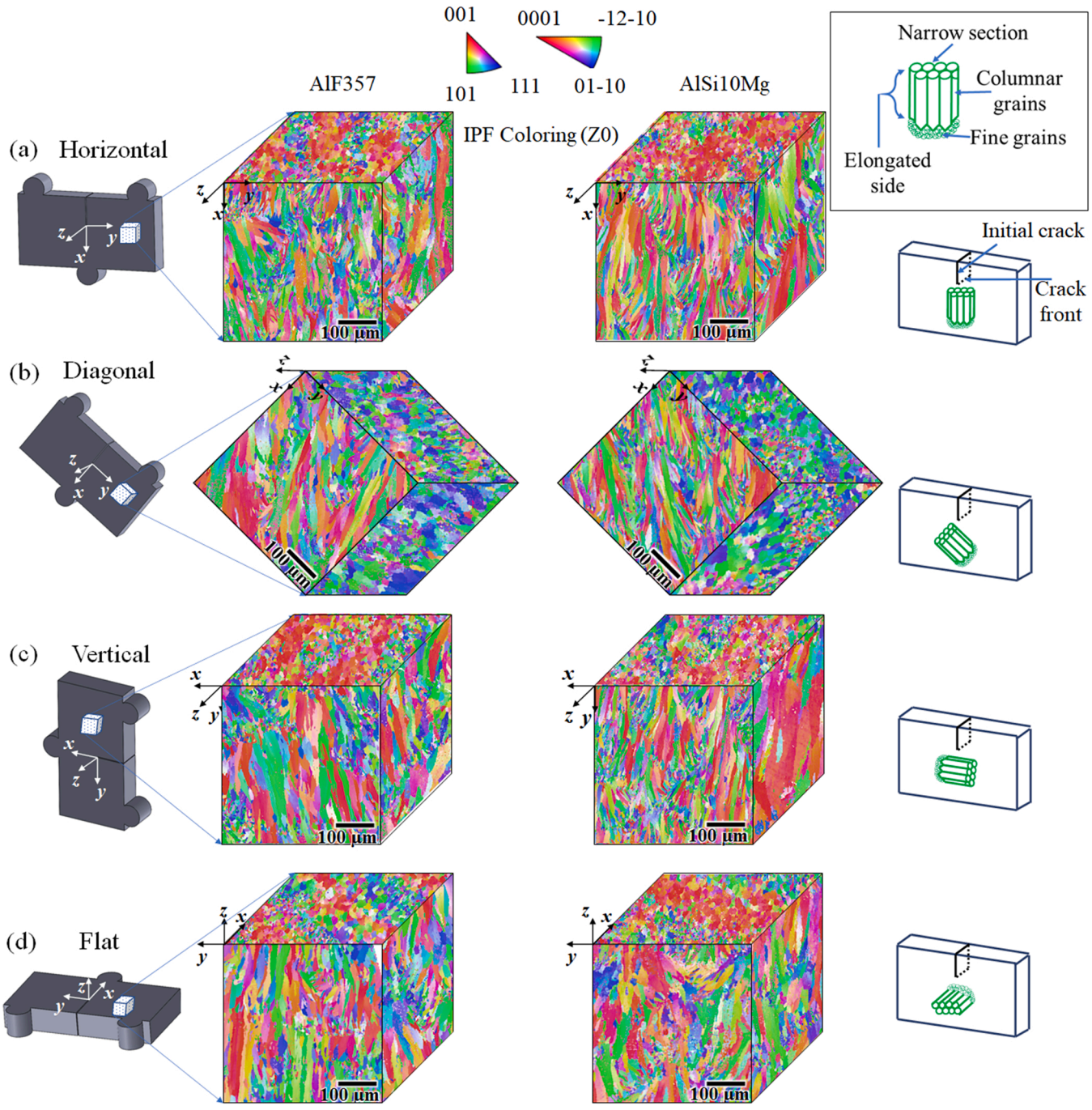

Fig. 12. 3D Microstructure of AlF357 and AlSi10Mg alloys for the (a) horizontal, (b) diagonal, (c) vertical, and (d) flat orientations as obtained from EBSD. (Note: *xyz* represents crack tip coordinates).

the loading pin in contact with the incident bar. However, *y*- or the *v*-field is observed to have contours symmetric in shape and antisymmetric in magnitude relative to the crack. Again, information on the hybrid DIC-FE methodology used and data extraction procedure is provided in Appendix-A for completeness. The region from which the *J*-integral values were evaluated in the dynamic experiments is highlighted in the speckle image shown in Fig. 8(a).

For each deformed image, the crack tip location was determined manually with the help of the displacement fields and the speckle images. By obtaining the crack tip location during the crack growth phase, the crack length histories were obtained and plotted (see Fig. 9). The crack growth rate was rather linear for both Al alloys. The build orientations seem to affect the crack speed only marginally with the flat built specimens showing a higher crack velocity relative to the horizontal counterparts. In AlF357, the flat orientation had an average crack velocity of 100 m/s, while the average crack velocity of the horizontal orientation was 86 m/s. In the case of AlSi10Mg, the average crack velocity of flat and horizontal orientations was 102 m/s and 86 m/s, respectively. The percentage error in the velocities was ~5%. More importantly, one can notice that the crack velocity was rather low and was found to be ~3% relative to the shear wave speeds of ~3100 m/s for both alloys. This observation allowed extraction of fracture parameters using steady-state assumptions even though the *J*-integral concept is strictly not applicable to highly transient events.

The dynamic crack growth resistance curves for both aluminum alloys are shown in Fig. 10. For the AlF357 alloy (Fig. 10(a)), the critical

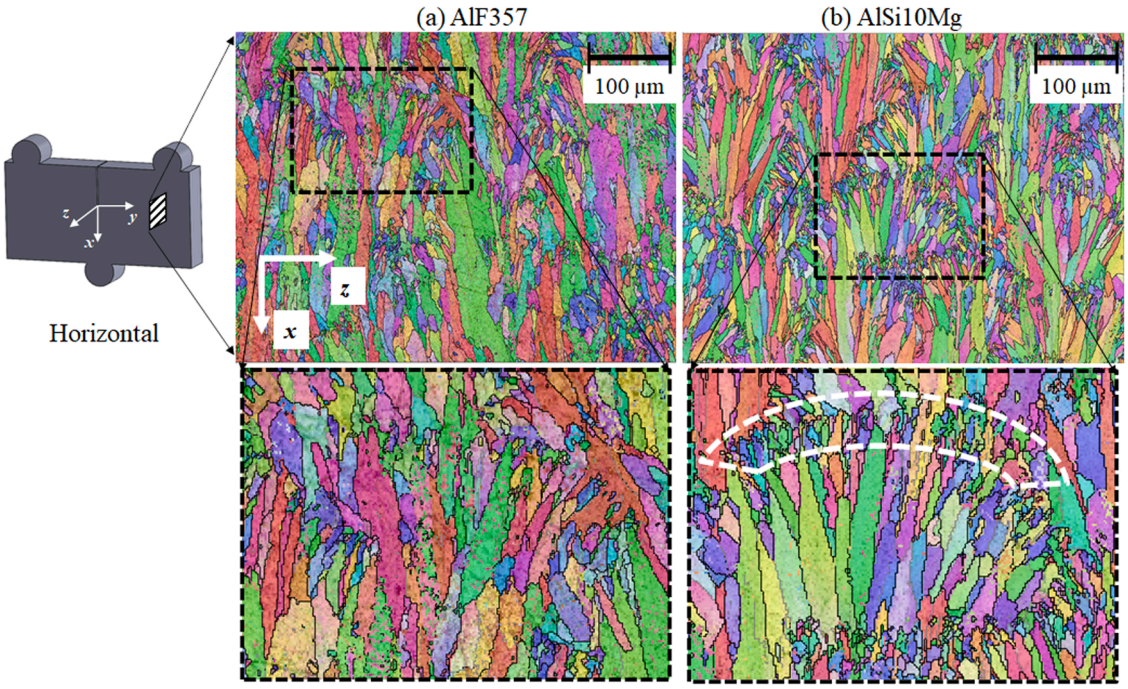

Fig. 13. EBSD images of *x*-*z* plane for the horizontal orientation of (a) AlF357 and (b) AlSi10Mg alloys. (Note: *xyz* correspond to crack tip coordinates).

energy release rate was the highest for the diagonal orientation at 18.9 kJ/m^2, followed by the horizontal orientation at 18.8 kJ/m^2, then the vertical one at 18.4 kJ/m^2 and lastly the flat orientation at 17.8 kJ/m^2. After crack initiation, all four orientations had a similar behavior; a gradual drop in the energy release rate was observed with crack growth. However, the horizontal orientation was observed to have a marginally better performance during crack propagation. Since both horizontal and diagonal orientations had nearly the same critical energy release rates (the difference was within the measurement error (~4% or ± 0.6 kJ/m^2)), the horizontal orientation could be considered the best build orientation under dynamic loading conditions as well. For AlSi10Mg alloy (Fig. 10(b)), the critical energy release rate was the highest for the horizontal orientation at 17.2 kJ/m^2, followed by the diagonal orientation at 16.8 kJ/m^2, then followed by the vertical orientation at 16.5 kJ/m^2 and lastly the flat orientation at 16.1 kJ/m^2. During crack propagation, all four orientations were observed to have similar fracture behavior as discussed earlier for AlF357.

The *J*-integral histories for both materials under dynamic loading conditions are shown in Fig. 11. Each history shows a monotonic increase in the energy release rate until crack initiation (at $t = 0$ μs,) regardless of materials and build orientations. For AlF357 alloy from Fig. 11(a), horizontal and diagonal orientations show a steady-state behavior until approx. $t = 10$ μs after which the *J*-integral values begin to drop off gradually. However, this somewhat subtle post-initiation behavior is absent in the vertical and the flat orientations; that is, the values show a gradual drop-off right after initiation. For AlSi10Mg alloy (Fig. 11(b)), all four build orientations exhibit similar behavior after crack initiation where the *J*-integral values begin to drop. All other observations are similar to the ones made from the crack growth resistance curves in Fig. 10(b). Again, as observed in the quasi-static case, AlF357 had a higher critical energy release rate (~10%) when compared to AlSi10Mg and horizontal orientation was the best out of all orientations studied under dynamic loading. It should also be noted that three specimens in each condition were tested to establish experimental repeatability. A set of *J*-integral histories for the horizontal build is shown in Fig. A4 for each alloy.

3.3. Microstructure characterization and fractography

To explain the macroscale fracture behaviors under quasi-static and dynamic conditions, microstructural characterization was carried out using EBSD, as shown in Fig. 12. The microstructural comparison is shown for all three planes (with respect to the crack tip coordinates), for all four build orientations, and both alloys. The build orientation of the specimen relative to the build plate is shown in the first column of Fig. 12. The specimen schematic in the figure highlights the planes for which the microstructural characterization has been carried out. 3D microstructures for AlF357 and AlSi10Mg alloys are shown in the second and third columns of Fig. 12, respectively. For all the build orientations, the microstructure mainly consists of elongated columnar grains with refined fine grains around the melt-pool boundaries. These columnar grains, in which the grains appear elongated along the build direction toward the build plate, can be observed for both investigated alloys. This typical L-PBF microstructure containing elongated grains surrounded by finer grains was expected in both alloys. This AM-induced microstructure is due to the repeated rapid melting and subsequent rapid cooling associated with the L-PBF process. Similar microstructures with elongated grains have been observed for L-PBF AlSi10Mg previously [16, 32–34]. The average grain size for AlF357 was found to be 9.7 μm, 8.3 μm, 8.3 μm, and 9.2 μm for the horizontal, diagonal, vertical, and flat orientations, respectively, with a standard deviation of 3 μm. The average grain size for AlSi10Mg was found to be 8.8 μm, 8.1 μm, 9.0 μm, and 8.9 μm for the horizontal, diagonal, vertical, and flat builds, respectively, with a standard deviation of 3 μm.

Fig. 12 also shows the *x*-*z* plane (with respect to the crack tip coordinates) for all the build orientations of both Al alloys. Note that the *x*-*z* plane corresponds to the crack propagation plane in all specimens. To further clarify the melt-pool direction and orientation of columnar grains with respect to the crack front, the schematics shown in the fourth column of Fig. 12 illustrate the direction of columnar grains and melt-pool boundary relative to the crack front for different build orientations. A schematic visualizing the terminologies related to microstructure is provided as an inset in Fig. 12. It can be noted that the columnar grains in the horizontal orientation were oriented parallel to the initial crack and the melt-pool boundary was perpendicular to the crack front.

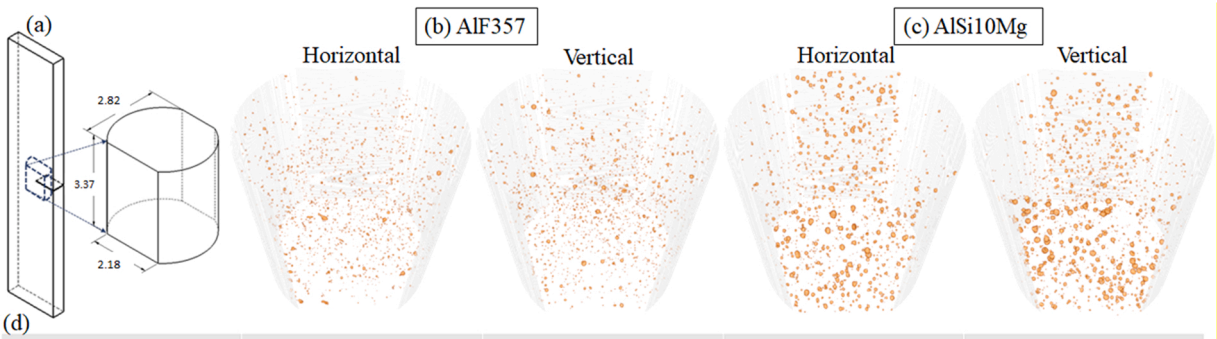

	(b) AlF357 Horizontal	(b) AlF357 Vertical	(c) AlSi10Mg Horizontal	(c) AlSi10Mg Vertical
Number of defects	2606	2615	1587	1864
Average Defect Volume (μm³)	2222	3066	17742	17979
(100-Density) %	0.021	0.029	0.102	0.121

Fig. 14. XCT results for the shown volume in (a) around the crack tip for the horizontally and vertically oriented quasi-static specimens fabricated from (b) AlF357 and (c) AlSi10Mg alloys. Results from the quantitative analysis are tabulated in (d). All dimensions are in mm.

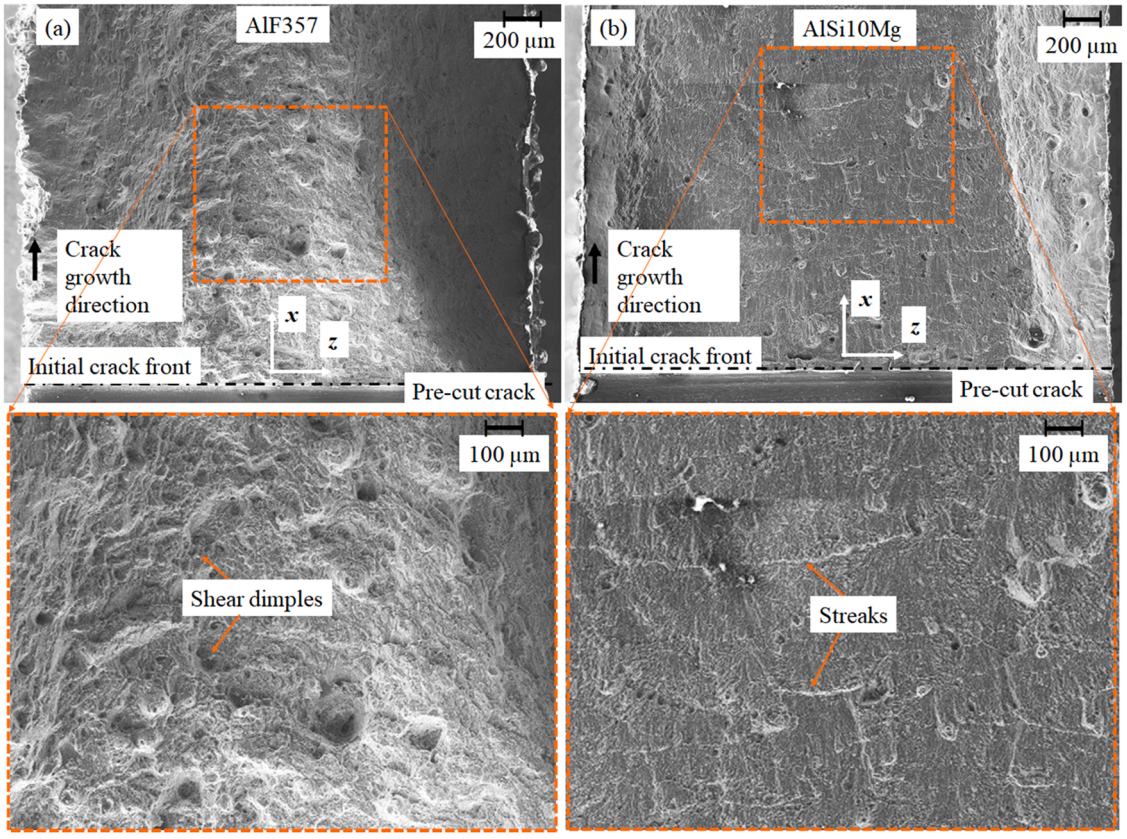

Fig. 15. SEM images of quasi-static fracture surfaces for the horizontal build orientation for (a) AlF357 and (b) AlSi10Mg alloys.

The opposite was observed in the vertical orientations where the columnar grains were perpendicular and the melt-pool boundary was parallel to the crack front. In the case of diagonally built specimens, the columnar grains and melt-pool boundary were at ~45° to the crack front. The flat orientation has a unique microstructure where all the grains oriented themselves along the thickness direction of the specimen. Hence, the initial crack cuts across the narrow section of the columnar grain whereas the crack front is aligned with the elongated direction of the columnar grain. Note that the melt-pool illustration is not to scale.

Fig. 13 shows one set of EBSD images of the *xz*-plane from the horizontal build orientation for both alloys. The elongated side of the columnar grains and the fine grains present in the melt-pool boundary are noticeable. The magnified image in Fig. 13(b) highlights the melt-pool boundary and the fine grains present in the boundary with a dashed white border.

Fig. 14 shows XCT results obtained for the horizontal and vertical orientations of quasi-static specimens for both alloys. A small volume around the crack tip was scanned to investigate the process-induced defects around the crack tip. A circular cylindrical volume of radius 3.37 mm whose center coincided with the center of the crack front was chosen and the locations where the cylinder fell outside the actual

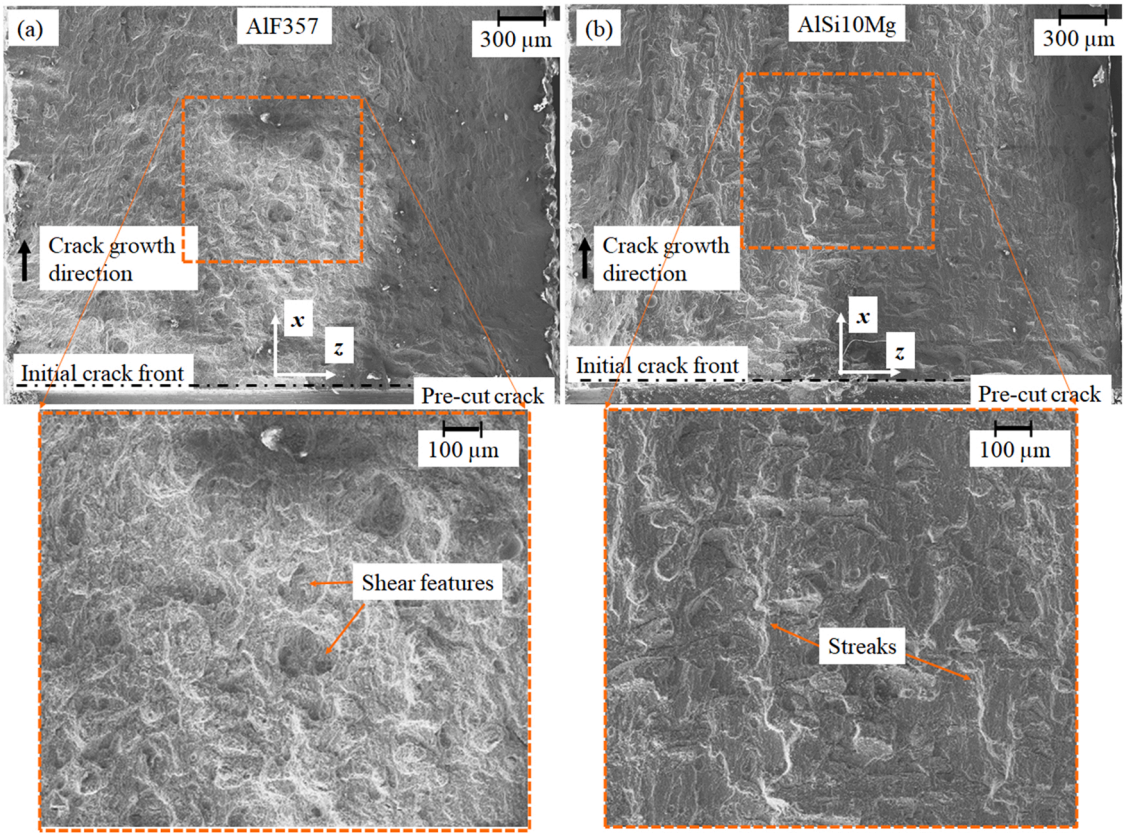

Fig. 16. SEM images of dynamic fracture surfaces for the horizontal build orientation for (a) AlF357 and (b) AlSi10Mg alloys.

surface of the specimen in the thickness direction (*z*-axis in the crack tip coordinate system) were eliminated from the scan. The resulting scanned volume is shown schematically in Fig. 14(a). The defect distribution results are shown in Fig. 14(b) and (c) and quantitative information is tabulated in Fig. 14(d) for each alloy. A greater number of defects was found in the case of AlF357. However, the average defect volume in AlF357 was eight times smaller than that of AlSi10Mg. Of the two build orientations compared, the horizontal orientation had a smaller number of defects and smaller average defect volume when compared to the vertical counterparts in either alloy. The values of (100-density) as a percentage clearly showed that the AlF357 was a denser alloy relative to AlSi10Mg and that the horizontal orientation was denser than the vertical orientation for each alloy.

Fig. 15 shows the SEM images of fractured surfaces of horizontally built AlF357 and AlSi10Mg specimens under quasi-static loading. Upon observation, it can be seen that the fracture surface of the AlF357 specimen (Fig. 15(a)) is much more textured than the AlSi10Mg counterpart. The texture and features of AlF357 containing dimples in the former are akin to ductile fracture events. These dimples are found to be uniformly distributed over the entire cross-section. The capability of the L-PBF process to produce homogeneous microstructure is believed to be responsible for these uniform ductile shear dominant dimples. For the AlSi10Mg specimen (Fig. 15(b)), however, the surface texture is relatively smooth and devoid of noticeable ductile failure features; only a few horizontal streaks perpendicular to the crack growth direction can be seen on the fracture surface. The length of these streaks in AlSi10Mg alloy, when compared to the dimples in AlF357, is relatively small and correlates well with the macroscale fracture parameters extracted. Similar fracture modes were observed under quasi-static loading for the diagonal, vertical, and flat orientations, and hence, for the sake of brevity, they are not shown.

Fig. 16 shows the fractured surface of the horizontally built AlF357 and AlSi10Mg specimens subjected to dynamic loading. A similar surface texture could be observed for both AlF357 and AlSi10Mg alloys. Again, a higher number of features representing shear failure could be observed on the AlF357 specimen cross-section when compared to the AlSi10Mg counterpart indicating a superior fracture behavior of AlF357 relative to AlSi10Mg. Furthermore, the bands formed in AlSi10Mg specimens are aligned vertically, along the crack growth direction. Considering that crack growth with negative dJ/da occurred immediately after crack initiation in AlSi10Mg, the fracture surface features seem to support the macroscale fracture behaviors observed in Figs. 10 and 11. The vertical bands correspond to the locations in which fracture initiated and the flat regions surrounding the bands indicate that brittle crack growth occurred after initiation. Again, similar fracture modes were observed under dynamic loading for the diagonal, vertical, and flat orientations and hence, are not shown here for the sake of brevity.

4. Discussion

4.1. Role of build orientation under quasi-static loading

The build orientation had a significant effect on the fracture behavior of both Al alloys under quasi-static loading. The horizontal orientation was found to be the best build orientation for both alloys, whereas the flat orientation was the least favorable in terms of macroscale crack initiation and growth parameters. In AlF357, the horizontal and diagonal orientations had ~70% higher values of critical energy release rate relative to the flat orientation. The same for the vertical orientation was ~10% higher when compared to the flat orientation. In terms of post-initiation fracture response, the horizontal, diagonal, and vertical orientations had ~190%, ~120%, and ~30% higher energy absorption relative to the flat orientation, respectively. In AlSi10Mg prints, the horizontal, diagonal, and vertical orientations had, respectively, ~55%, ~50%, and ~20% higher energy release rates at crack initiation relative to the flat orientation. In the crack propagation regime, the energy

absorbed by the horizontal, the diagonal, and the vertical orientations was ~200%, ~100%, and ~80% more than the flat orientation, respectively. The variations between different orientations could be explained from the microstructures (Fig. 12). The high number of elongated grains and the perpendicular melt-pool boundaries along the mode-I crack in the horizontal orientation enhanced the critical energy release. In the diagonal orientation, the crack still has to overcome inclined melt-pool boundaries. However, the elongated side of the columnar grains encountered during crack propagation is not as high as in the horizontal case. For the vertical build orientation, the crack can initiate and propagate among the narrow section of the columnar grains. The melt-pool boundary being parallel to the crack in the vertical orientation offers little-to-no resistance. In the flat orientation specimens, the initial crack is aligned with the narrow section of the grains, whereas the crack front is parallel to the elongated side. Hence, similar to the vertical orientation, the crack can initiate and propagate among the narrow section of the columnar grains with less resistance. The difference between the vertical orientation and the flat orientation could be attributed to the relative orientation of the crack front to the elongated side of the columnar grains. In the vertical orientation, the crack front is orthogonal to the elongated side of the grains, whereas in the flat orientation, the crack front is aligned with the elongated side.

The XCT results shown in Fig. 14 offer further insight into the variation in the fracture behavior of the horizontal and vertical specimen orientations under quasi-static loading conditions. The higher number of defects and increased average defect volume found in the vertical orientation lower its critical energy release rate when compared to the horizontal counterpart.

The effect of build orientation was more significant in AlF357 when compared to AlSi10Mg. The critical J-integral values under quasi-static loading had a variation of ~4.0 kJ/m^2 for AlF357 between the build orientations, while it was ~1.3 kJ/m^2 for AlSi10Mg. Less difference in the effect of the build orientations on the quasi-static fracture behavior of AlSi10Mg could be attributed to the homogeneous distribution of columnar grains inside the melt-pool. From the x-z planes shown in Fig. 13, it could be observed that the AlSi10Mg melt-pools have their columnar grains radially distributed toward the melt-pool boundary, which is not evident in the EBSD images of AlF357 specimens.

AlF357 alloy exhibited better fracture performance (~30%) than AlSi10Mg alloy. AlF357 has a higher YS (by ~10%) and tensile stress-strain response compared to AlSi10Mg [30,31]. In addition to this, differences in the chemical composition, especially the silicon content (i.e., AlF357 has <7.5% weight content of silicon, whereas AlSi10Mg has <11%) which form the brittle intercellular silicon network [14,16] in the microstructure after the stress relief cycle could have attributed to the lower fracture performance of AlSi10Mg specimens. In addition, the volumetric information about the defect size and distribution obtained from XCT results (Fig. 14) showed that AlF357 was a denser material than AlSi10Mg. That is, the porosity/defect density in AlSi10Mg was higher and hence, the presence of the increased pores and defects could have further reduced the fracture performance.

4.2. Role of build orientation under dynamic loading

The build orientation did not significantly affect the dynamic fracture behavior of the L-PBF Al alloys studied. In AlF357, the largest difference in critical energy release rate between the diagonal and flat orientations was ~6%. In AlSi10Mg, the horizontal and the flat orientations had the largest difference of ~7%. The experimental errors in the dynamic experiments were approximately 4%. Hence, it can be concluded that the dynamic fracture behavior of these two alloys is not significantly dependent on the build orientation. However, AlF357 alloy outperformed AlSi10Mg in terms of fracture behavior by ~10%. Again, the difference in YS of AlF357 compared to AlSi10Mg may be responsible for the observed fracture behaviors between the two alloys. The marginal difference between the build orientations could again be attributed to the elongated grain directions as discussed earlier for the quasi-static cases.

4.3. Role of loading rate on fracture behavior

Both AlF357 and AlSi10Mg were found to have significant strain-rate sensitivity in terms of critical fracture parameters. Dynamically loaded AlF357 specimens (strain-rate of ~500 s^{-1}) had on average ~175% higher critical energy release rate when compared to the behavior under quasi-static (strain-rate ~10^{-4} s^{-1}) loading. This difference was around ~200% for AlSi10Mg specimens. The main reason for such a substantial increase is the change in crack initiation/fracture mechanism. The quasi-static loading provided sufficient time for ductile failure mechanisms to become activated as evident from crack propagation history and relatively poor failure response. This can be observed from the SEM fractographs in Figs. 15 and 16. In these, shear lips adjacent to $z/B = \pm 0.5$ (B being specimen thickness) can be seen in the quasi-static loading cases, whereas a relatively flat fracture surface is evident in dynamically loaded specimens. As evident from the XCT results, there exists a considerable number of volumetric defects of varying size in both alloys. Mobility of dislocations and manifestation of such volumetric defects in Al specimens have potentially led to ductile failures and the formation of shear flanks in quasi-static cases. The same failure mechanisms may not have had sufficient time to become activated in the dynamic counterparts resulting in a relatively brittle fracture behavior in terms of fracture surface morphology. This change of fracture mechanism was reported to increase the dynamic mechanical properties of L-PBF AlSi10Mg alloy by a factor of 2 in high strain-rate loading in a previously published work [21] and the results here seem consistent with that observation.

5. Conclusion

In this work, fracture parameters for AlF357 and AlSi10Mg aluminum alloy specimens fabricated by the L-PBF process were quantified. The effect of four different build orientations (horizontal, diagonal, vertical, and flat) and two distinct strain-rates (quasi-static and dynamic) were studied. The AM specimens were statically and dynamically loaded using a mechanical tester and a Kolsky bar apparatus. Surface deformations near crack tip vicinity in all specimens were mapped using the digital image correlation method. High-speed photography was employed to capture the dynamic loading events. A hybrid DIC-FE methodology was adopted to extract energy release rates in the pre- and post-crack initiation phases of a pre-cut notch. Microstructural characterization and fractography were also undertaken to explain the macroscale fracture parameters. The major conclusions of this work are as follows:

- AlF357 alloy was found to show better fracture performance than AlSi10Mg alloy under both quasi-static and dynamic loading conditions with consistently higher critical energy release rate values.
- Specimen build orientation had a significant effect on the fracture behavior of both L-PBF Al alloys under quasi-static loading. The horizontal orientation was found to be the best build orientation for both alloys, while the flat orientation was the least favorable in terms of critical energy release rate and crack growth resistance behavior. The relative orientation of the elongated grains and the fine grains found in the melt-pool boundary with respect to the mode-I crack path contributed to the difference observed in macroscale fracture behavior among the four build orientations studied.

- The effect of build orientation on the fracture behavior of L-PBF AlF357 and AlSi10Mg alloys under dynamic loading was negligible.
- A change in the fracture mechanism was observed with the change in strain-rate. L-PBF AlF357 and AlSi10Mg alloys were found to have on average ~175% and ~200% increase in critical energy release rate under dynamic loading conditions when compared to quasi-static counterparts. The temporal advantage for dislocations to mobilize and defects to manifest during quasi-static conditions activate many different failure mechanisms during quasi-static fracture.

CRediT authorship contribution statement

Nima Shamsaei: Writing – review & editing, Supervision, Resources, Formal analysis, Conceptualization. **Ankit Saharan:** Writing – review & editing, Resources. **Hareesh V Tippur:** Writing – review & editing, Writing – original draft, Visualization, Supervision, Resources, Project administration, Methodology, Investigation, Conceptualization. **John P Isaac:** Writing – review & editing, Writing – original draft, Visualization, Validation, Software, Methodology, Investigation, Formal analysis, Data curation. **Spencer Thompson:** Writing – review & editing, Resources. **Seungjong Lee:** Writing – review & editing, Visualization, Validation, Investigation, Formal analysis, Data curation.

Declaration of Competing Interest

The authors declare that they have no known competing financial interests or personal relationships that could have appeared to influence the work reported in this paper.

Data Availability

Data will be made available on request.

Acknowledgments

The authors would like to thank EOS North America for providing the additively manufactured aluminum alloy specimens used in this work.

Appendix-A

Hybrid DIC-FE method

During experiments, random speckle images were recorded using a digital camera in the reference (undeformed) and deformed states. These images were then segmented into subsets or sub-images of gray scales for carrying out DIC. The displaced location of each subset in the deformed state relative to its reference state was subsequently determined using a grayscale correlation algorithm. In doing so, the displacement data at the center of each subset was computed over the whole region of interest. To implement the proposed approach of computing the *J*-integral, the domain was discretized such that the locations where displacements were determined to match the nodal locations in the FE model consisting of a square grid of quadrilateral elements parallel and perpendicular to the dominant edges of the specimen. It should be noted, however, that when the crack propagated and followed a kinked path relative to its initial orientation, the neighborhood of the crack adjacent to the crack flanks was discretized along a narrow band and the interpolated displacements obtained from DIC subsets were input at the FE nodes. It should also be noted that the crack tip was modeled as a sharp discontinuity for simplicity. Since the measured displacements were used as input to the FE model to dictate the post-processing of DIC data and find the *J*-integral values, the sharpness of the crack tip in the model is unimportant.

A flowchart of the steps associated with the *J*-integral evaluation is shown in Fig. A1. First, the experimentally measured displacement components from DIC were imported as nodal boundary conditions for the FE discretization. The model was then run using Abaqus structural analysis software (v.16.1) after identifying the current crack tip position and its orientation relative to the previous to extract the energy release rate using in-built algorithms.

For all quasi-static experiments, ARAMIS® was used to perform grayscale correlation by segmenting images into a square sub-image of 25 pixels with 5 pixels step size between neighboring sub-images. The scale/magnification factor was ~12 μm/pixel for these images. The *J*-integral output from Abaqus is plotted as a function of contour numbers and *r/B* ratio and is shown in Fig. A2. The *J*-integral values obtained around the crack tip (*r/B* ratio < 0.3) typically have high (erratic) values because of factors such as crack tip stress triaxiality and inelastic deformations; thus, violating small-scale yielding assumptions. However, as the distance from the crack tip increases, the values stabilize and exhibit path independence. Once such a plateau region of constant values is identified, the *J*-integral values are then extracted as an average over the region. For the quasi-static experiments, as shown in Fig. A2(a), the constant *J*-integral values were averaged over contour numbers 16–75 or 1–4.5 mm (*r/B* ratio ~ 0.3–1.5; shaded region in Fig. 6(a)), at each load-step.

For the dynamic experiments, a square sub-image size of 25 pixels and a step size of 5 pixels was used. The scale factor, however, was ~30 μm/pixel. As shown in Fig. A2(b), the extracted *J*-integral values were averaged over contour numbers 10–33 or radial extent of 1.5–5 mm (*r/B* ratio ~ 0.4–1.3; shaded region in Fig. 8(a)). During the FE analysis phase of the approach, the material behavior of both aluminum alloys was represented using an elasto-plastic behavior (stress-strain curves are shown in Fig. A3) using uniaxial tensile test results made available from the datasheet supplied by EOS [30,31].

Based on the measured longitudinal wave speed (~6500 m/s) in AM AlF357 and AlSi10Mg alloys, a temporally steady state is expected to take hold in the dynamically loaded specimens after about ~12 μs which corresponds to approx. three stress wave round-trips [12,35] based on the geometry of the specimen. The time duration between the impact and crack initiation is ~80 μs, the data acquired and reported here belongs to the steady-state loading regime.

Fig. A4 shows the one set of repeatable *J*-integral histories for the horizontal build for both AlF257 and AlSi10Mg. Three specimens were tested in each condition for the quasi-static and dynamic fracture experiments to ensure experimental repeatability.

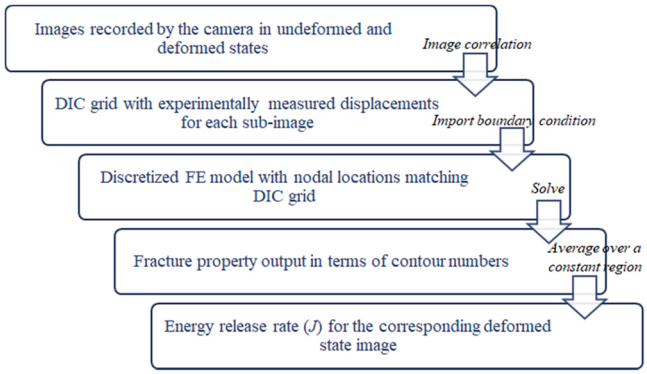

Fig. A1. Hybrid DIC-FE methodology flowchart.

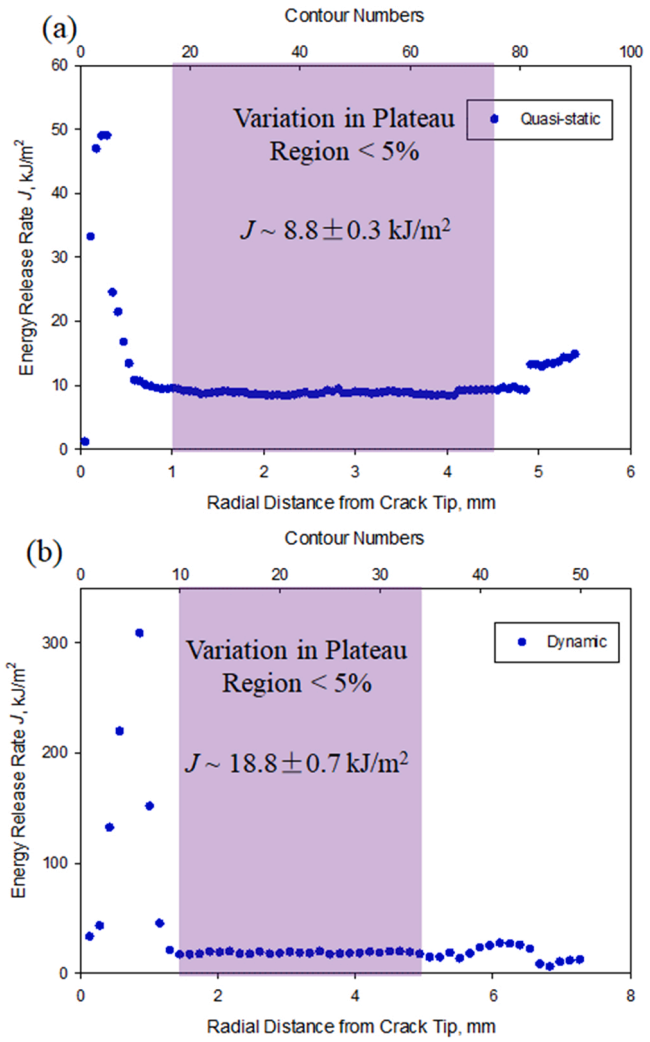

Fig. A2. Plot of J-integral values in terms of contour numbers and radial distance from the crack tip for horizontally built ALF357 alloy at crack initiation under (a) quasi-static and (b) dynamic loading.

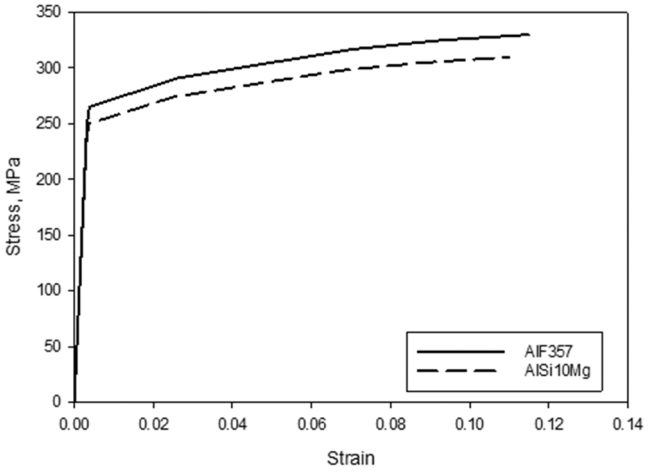

Fig. A3. Stress-strain curves for AM AlF357 and AlSi10Mg from EOS [30,31] used in FE for elasto-plastic analysis.

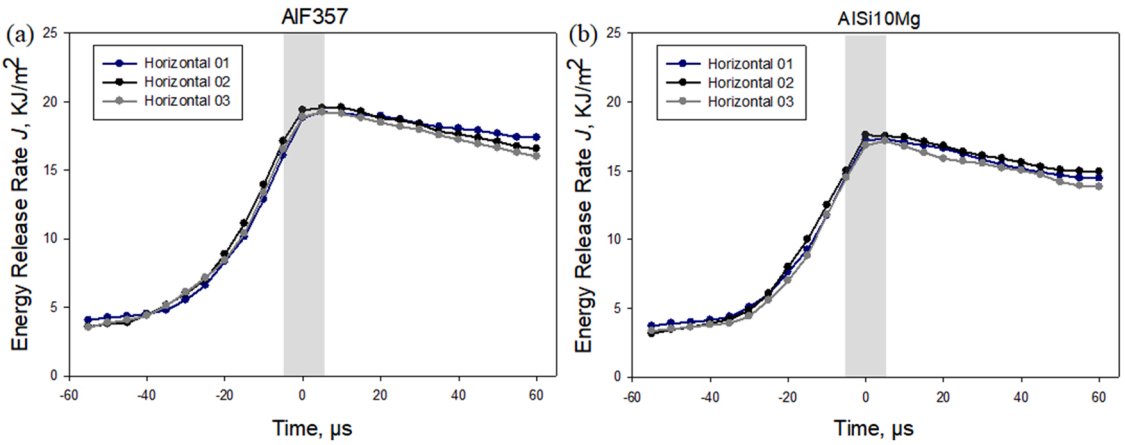

Fig. A4. Repeatable *J*-integral histories for (a) AlF357 and (b) AlSi10Mg alloys under dynamic loading for the horizontal build. Negative and positive time scales correspond to pre- and post- crack initiation regimes. The gray band centered on $t = 0$ μs refers to the approximate crack initiation instant.

References

[1] L.E. Murr, Frontiers of 3D printing/additive manufacturing: from human organs to aircraft fabrication†, J. Mater. Sci. Technol. 32 (10) (2016) 987–995.
[2] X. Wang, S. Xu, S. Zhou, W. Xu, M. Leary, P. Choong, M. Qian, M. Brandt, Y.M. Xie, Topological design and additive manufacturing of porous metals for bone scaffolds and orthopaedic implants: a review, Biomaterials 83 (2016) 127–141.
[3] K.H. Rendigs, Aluminium structures used in aerospace - status and prospects, Mater. Sci. Forum 242 (1997) 11–24.
[4] J. Ni, H. Ling, S. Zhang, Z. Wang, Z. Peng, C. Benyshek, R. Zan, A.K. Miri, Z. Li, X. Zhang, J. Lee, K.J. Lee, H.J. Kim, P. Tebon, T. Hoffman, M.R. Dokmeci, N. Ashammakhi, X. Li, A. Khademhosseini, Three-dimensional printing of metals for biomedical applications, Mater. Today Bio 3 (2019), 100024.
[5] H.W. Dong, Y. Sun, H. Qian, J.Q. Jian, Y. Shao, Z.D. Li, D.H. Zou, N.G. Liu, L. Wan, M.W. Wang, Y.J. Chen, J.H. Zhang, Progress in additive manufacturing on new materials: a review, J. Mater. Sci. Technol. 35 (2) (2019) 242–269.
[6] C. Cui, et al., Review on fabrication methods of in situ metal matrix composites, Cailiao Kexue Yu Jishu J. Mater. Sci. Technol. 16 (2000) 619–626.
[7] J.K. Park, A.J. Ardell, Microstructures of the commercial 7075 Al alloy in the T651 and T7 tempers, Metall. Trans. A 14 (10) (1983) 1957–1965.
[8] P.N. Adler, R. DeIasi, Calorimetric studies of 7000 series aluminum alloys: II. Comparison of 7075, 7050 and RX720 alloys, Metall. Trans. A 8 (7) (1977) 1185–1190.
[9] J. Zhang, et al., A review of selective laser melting of aluminum alloys: Processing, microstructure, property and developing trends, J. Mater. Sci. Technol. 35 (2) (2019) 270–284.
[10] W.E. Frazier, Metal additive manufacturing: a review, J. Mater. Eng. Perform. 23 (6) (2014) 1917–1928.
[11] Fulcher, B.A., D.K. Leigh, and T.J. Watt. Comparison of AlSi10Mg and Al 6061 processed through DMLS. 2014. University of Texas at Austin.
[12] E.D.H. Davies, S.C. Hunter, The dynamic compression testing of solids by the method of the split Hopkinson pressure bar, J. Mech. Phys. Solids 11 (3) (1963) 155–179.
[13] C.E. Roberts, D. Bourell, T. Watt, J. Cohen, A novel processing approach for additive manufacturing of commercial aluminum alloys, Phys. Procedia 83 (2016) 909–917.
[14] M. Muhammad, P.D. Nezhadfar, S. Thompson, A. Saharan, N. Phan, N. Shamsaei, A comparative investigation on the microstructure and mechanical properties of additively manufactured aluminum alloys, Int. J. Fatigue 146 (2021), 106165.
[15] S. Kenzari, D. Bonina, J. Marie Dubois, V. Fournée, Complex metallic alloys as new materials for additive manufacturing, Sci. Technol. Adv. Mater. 15 (2) (2014), 024802.
[16] P.D. Nezhadfar, S. Thompson, A. Saharan, N. Phan, N. Shamsaei, Structural integrity of additively manufactured aluminum alloys: effects of build orientation on microstructure, porosity, and fatigue behavior, Addit. Manuf. 47 (2021), 102292.
[17] K. Kempen, L. Thijs, J. Van Humbeeck, J.P. Kruth, Mechanical properties of AlSi10Mg produced by selective laser melting, Phys. Procedia 39 (2012) 439–446.
[18] U. Tradowsky, et al., Selective laser melting of AlSi10Mg: Influence of post-processing on the microstructural and tensile properties development, Mater. Des. 105 (2016) 212–222.
[19] L.C. Araújo, A.H.G. Gabriel, E.B. da Fonseca, J.A. Avila, A.L. Jardini, R. Seno Junior, É.S.N. Lopes, Effects of build orientation and heat treatments on the tensile and fracture toughness properties of additively manufactured AlSi10Mg, Int. J. Mech. Sci. 213 (2022), 106868.
[20] I. Rosenthal, A. Stern, N. Frage, Strain rate sensitivity and fracture mechanism of AlSi10Mg parts produced by Selective Laser Melting, Mater. Sci. Eng.: A 682 (2017) 509–517.
[21] E. Zaretsky, A. Stern, N. Frage, Dynamic response of AlSi10Mg alloy fabricated by selective laser melting, Mater. Sci. Eng.: A 688 (2017) 364–370.
[22] B. Nurel, M. Nahmany, N. Frage, A. Stern, O. Sadot, Split hopkinson pressure bar tests for investigating dynamic properties of additively manufactured AlSi10Mg alloy by selective laser melting, Addit. Manuf. 22 (2018) 823–833.
[23] T. Maconachie, M. Leary, J. Zhang, A. Medvedev, A. Sarker, D. Ruan, G. Lu, O. Faruque, M. Brandt, Effect of build orientation on the quasi-static and dynamic response of SLM AlSi10Mg, Mater. Sci. Eng.: A 788 (2020), 139445.
[24] M. Laurençon, T. de Rességuier, D. Loison, J. Baillargeat, J.N.D. Ngnekou, Y. Nadot, Effects of additive manufacturing on the dynamic response of AlSi10Mg to laser shock loading, Mater. Sci. Eng.: A 748 (2019) 407–417.
[25] G. Dai, Z. Peng, Q. Zhang, W. Zhou, M. Xia, H. Li, A. Pan, Q. Wan, B. Zou, Two-dimensional digital image correlation for in-plane displacement and strain measurement: a review, Meas. Sci. Technol. 20 (6) (2009), 062001.
[26] J.P. Isaac, S. Dondeti, H.V. Tippur, Crack initiation and growth in additively printed ABS: Effect of print architecture studied using DIC, Addit. Manuf. 36 (2020), 101536.
[27] J.P. Isaac, S. Dondeti, H.V. Tippur, Fracture behavior of additively printed ABS: effects of print architecture and loading rate, Int. J. Solids Struct. 212 (2021) 80–95.
[28] J.P. Isaac, S. Lee, N. Shamsaei, H.V. Tippur, Dynamic fracture behavior of additively manufactured Scalmalloy®: Effects of build orientation, heat-treatment and loading-rate, Mater. Sci. Eng.: A 826 (2021), 141978.
[29] A.T. Owens, H.V. Tippur, Measurement of mixed-mode fracture characteristics of an epoxy-based adhesive using a hybrid digital image correlation (DIC) and finite elements (FE) approach, Opt. Lasers Eng. 140 (2021), 106544.
[30] EOS. Material Data Sheet EOS Aluminium AlF357 Light Weight & Corrosion resistance. 2019.
[31] EOS. Material data sheet: EOS AlSi10Mg. 2014.
[32] F. Trevisan, F. Calignano, M. Lorusso, J. Pakkanen, A. Aversa, E.P. Ambrosio, M. Lombardi, P. Fino, D. Manfredi, On the Selective Laser Melting (SLM) of the AlSi10Mg alloy: process, microstructure, and mechanical properties, Materials 10 (2017) 1.
[33] D. Manfredi, F. Calignano, M. Krishnan, R. Canali, E.P. Ambrosio, E. Atzeni, From powders to dense metal parts: characterization of a commercial AlSiMg alloy processed through direct metal laser sintering, Materials 6 (2013) 3–869.
[34] D. Manfredi, et al., Additive manufacturing of Al alloys and aluminium matrix composites (AMCs). Light Metal Alloys Applications, InTech, 2014.
[35] K. Xia, W. Yao, Dynamic rock tests using split Hopkinson (Kolsky) bar system – a review, J. Rock. Mech. Geotech. Eng. 7 (1) (2015) 27–59.